Hyperthermal Oxygen Interacting with Silicon Surfaces: Adsorption, Implantation, and Damage Creation

E. C. Neyts,*[†] U. Khalilov,[†] G. Pourtois,[†,‡] and A. C. T. van Duin[§]

[†]Department of Chemistry, PLASMANT Research Group, University of Antwerp, Universiteitsplein 1, B-2610 Wilrijk-Antwerp, Belgium

[‡]IMEC, Kapeldreef 75, B-3001 Leuven, Belgium

[§]Department of Mechanical and Nuclear Engineering, Penn State University, University Park, Pennsylvania 16801, United States

S *Supporting Information*

ABSTRACT: Using reactive molecular dynamics simulations, we have investigated the effect of single-impact, low-energy (thermal-100 eV) bombardment of a Si(100){2 × 1} surface by atomic and molecular oxygen. Penetration probability distributions, as well as defect formation distributions, are presented as a function of the impact energy for both species. It is found that at low impact energy, defects are created chemically due to the chemisorption process in the top layers of the surface, while at high impact energy, additional defects are created by a knock-on displacement of Si. These results are of particular importance for understanding device performances of silica-based microelectronic and photovoltaic devices.
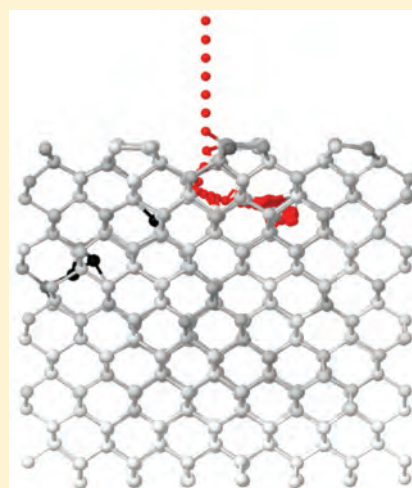
INTRODUCTION

The growth of ultrathin (<2 nm) silica layers on Si-crystals near room temperature is an important issue in the fabrication of microelectronics and photovoltaic devices.[1−6] In such thin films, a significant portion of the film is occupied by the transition layer at the Si/SiO$_2$ interface, degrading the dielectric properties, the light absorption efficiency, and hence the performances of the devices. Resolving this issue requires understanding of especially the initial stage of the Si-oxidation process at the atomic level. The formation of such a thin oxide film at room temperature is possible using a laser detonation hyperthermal (i.e., in the energy range 1−15 eV) atomic beam source.[7,8] Furthermore, the reaction behavior of hyperthermal oxygen on silicon-based materials is also of importance for spacecraft traveling through the low-Earth orbital, in which the dominant component is atomic oxygen.[8,9] Hence, there is a considerable interest in the study of the interaction of hyperthermal oxygen with Si at low temperature (i.e., below and near room temperature).

The reaction behavior of oxygen during the initial oxidation stage of Si(100) has been investigated both experimentally[10−17] and theoretically.[18,19] It is generally accepted that the adsorption probability of thermal oxygen atoms at room temperature is much higher than that of molecular oxygen.[2,10−13,20,21]

Molecular adsorption has a rather low probability, on the order of 0.0002−0.2, which decreases with increasing incident energy in the thermal energy regime due to the trapping ability of the surface.[14,15] At thermal energy, molecular oxygen frequently scatters, while in the hyperthermal energy regime, dissociative scattering, atom abstraction, and charge transfer are often observed.[4,5,21]

Although various theoretical and experimental studies are devoted to investigate the initial oxidation process of Si, the probabilities for penetration, desorption, and implantation during this stage have not yet been investigated in full detail.[17,22] Mechanisms of adsorption and desorption have previously been analyzed by first-principles calculations.[18,19,23] Due to computational limits, however, these calculations cannot probe, e.g., implantation probability distributions or defect formation at higher impact energies. Therefore, in this paper, we apply reactive molecular dynamics (MD) simulations to investigate the impact behavior of both atomic and molecular oxygen as a function of impact energy on a pristine Si(100){2 × 1} surface near room temperature.

■ COMPUTATIONAL DETAILS

1. Description of the Interatomic Potential. MD simulations are used to trace the impact behavior of oxygen on the silicon surface. In a MD simulation, the path of the atoms is followed through space and time by integrating the equations of motion. Forces on the atoms are derived from a suitable interatomic potential.

Here, we employ the Reax force field (ReaxFF) potential.[24] This potential uses the bond order/bond distance relationship formally introduced by Abell.[25] Bond orders, summed from σ, π, and $\pi\pi$ contributions, are calculated instantaneously from interatomic distances

$$BO_{ij} = BO_{ij}^{\sigma} + BO_{ij}^{\pi} + BO_{ij}^{\pi\pi}$$

$$= \exp\left[p_{bo1}\left(\frac{r_{ij}}{r_0^{\sigma}}\right)^{p_{bo2}}\right] + \exp\left[p_{bo3}\left(\frac{r_{ij}}{r_0^{\pi}}\right)^{p_{bo4}}\right]$$

$$+ \exp\left[p_{bo5}\left(\frac{r_{ij}}{r_0^{\pi\pi}}\right)^{p_{bo6}}\right]$$

where r_{ij} is the scalar distance between atoms i and j, r_0 is the equilibrium distance, and $p_{bo1}-p_{bo6}$ are fitting parameters. Overcoordination and undercoordination energy penalties are then used to enforce the correct bond order. The total system energy is the sum of several partial energy terms that include lone pairs, undercoordination, overcoordination, valence and torsion angles, conjugation, hydrogen bonding, as well as van der Waals and Coulombic interactions. Because Coulombic and van der Waals interactions are calculated between every pair of atoms, the ReaxFF potential describes not only covalent bonds but also ionic bonds and the whole range of intermediate interactions. Charge distributions are calculated based on geometry and connectivity using the electronegativity equalization method (EEM).[26] The force field parameters were optimized to reproduce ab initio data using a single-parameter search optimization technique as described previously.[27] A detailed description of the force field development for the Si/O system can be found in refs 28 and 29. The Si/O force field has previously been applied successfully for the study of self-assembly of silica nanocages.[30] Recently, a version extended to include hydrogen was applied to the silica—water interface.[31] Also, recently the applicability of ReaxFF to the reactive interaction of oxygen with surfaces has been demonstrated for Pt(111) surfaces.[32] Currently, the ReaxFF potential is capable of describing nearly half of the periodic table of the elements and their compounds, including hydrocarbons, silicon/silicon oxide, metals, metal oxides, and metal hydrides, see, e.g., ref 33 and references therein.

2. Description of the Simulations. Prior to oxygen impact, the Si(100){2 × 1} surface was treated as follows: first, the surface is equilibrated at 333 K using the Berendsen heat bath (NVT dynamics). Then, the obtained structure is relaxed in the microcanonical ensemble for 5 ps. The radial distribution function of the resulting structure shows peaks at 2.32, 3.77, and 4.46 Å, which is in good correspondence with the experimental values of 2.35, 3.84, and 4.50 Å.[34] A side view and top view of the resulting structure are shown in Figure 1.

Oxygen impacts are performed using the following procedure: the incident particle (oxygen atom or oxygen molecule) is positioned at 5 Å above the highest Si-atom of the crystal, perpendicular to the surface, while its location in the surface plane is
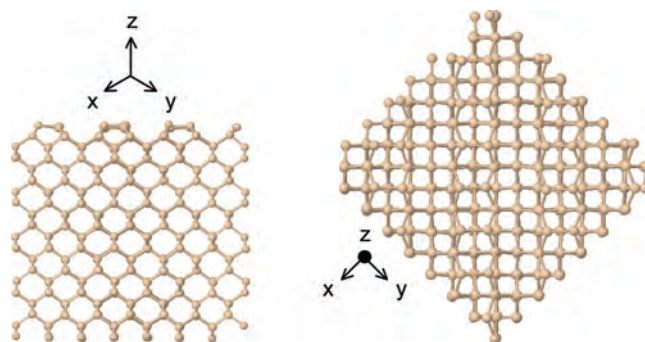
Figure 1. Side view and top view of the Si(100){2 × 1} substrate.
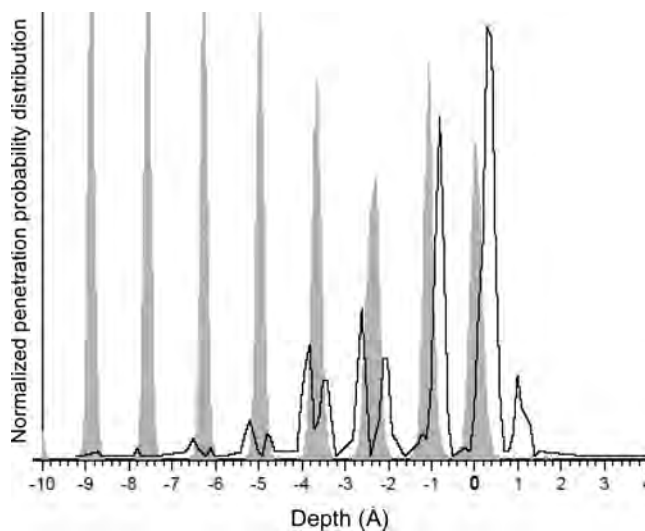
Figure 2. Calculated normalized penetration probability distributions of oxygen atoms, after the impact of atomic or molecular oxygen on Si(100){2 × 1}.

chosen randomly. In the case of molecular oxygen, the O_2 molecule is rotated randomly prior to impact. Depending on the oxygen source, the impinging particle is either launched randomly at the surface, in the thermal case, or directed normal to the surface to describe the laser detonation for the hyperthermal impacts.[7,8] All impacts are nonconsecutive, i.e., each impact occurs on a pristine Si-surface, and monitored for 3 ps. The impinging particle was bound to a kinetic energy equal to 0.028 (here below referred as thermal), 1, 5, 10, 31.6, 50, and 100 eV, and each case is repeated 1000 times to gather statistically valid results.

■ RESULTS AND DISCUSSION

1. Oxygen Penetration Probability Distributions. In Figure 2, the penetration probability distributions are shown for atomic and molecular oxygen as a function of the impacting energy on the Si(100){2 × 1} surface at 333 K. Interestingly, the chemisorption process of O_2 is found, in all cases, to be dissociative, which implies that, even in the case of the impact of molecular oxygen, the O radicals penetrate the surface. In the low-energy regimes (thermal and 1 eV), the deposition behavior is very similar for the atomic and the molecular forms: after impact, most of the oxygen atoms are located in the uppermost Si-layer and the first subsurface layer (note that in the case of the

Table 1. Maximum Depth Reached by the Hyperthermal Oxygen Atoms after Impact (by Atomic or Molecular Oxygen), for Different Incident Energies

incident energy (eV)	maximum depth (Å) (O impacts)	maximum depth (Å) (O_2 impacts)
5.0	9.0	8.0
10.0	9.5	9.0
31.6	13.0	12.0
50.0	14.0	14.5
100.0	26.0	19.5

$\{2 \times 1\}$ reconstruction of Si(100), the atoms belonging to the first and about half of the atoms of the second subsurface layer are not covered by the surface atoms). The oxygen atoms are found to migrate from the topmost layer to a back-bond center (after dissociation in the case of O_2), in good agreement with previous reports based on first-principles simulations.[18] Most atoms cannot move deeper into the bulk due to the associated activation energy barrier, which is on the order of 1 eV.[13,18]

In the hyperthermal energy regime, on the other hand, this energy barrier (estimated to be about 1.0 and 2.4 eV[18]) can be surmounted, and the incoming atoms can penetrate deeper than the first or second subsurface layers (located at about 1.1 and 2.4 Å below the surface, respectively), as illustrated by the calculated surface depth reached by the oxygen atoms as a function of the kinetic energy provided (Table 1). Note that the change in maximum penetration depth as a function of incident energy is smaller for the molecular impacts than for the atomic oxygen one due to the immediate breakup upon collision of the molecules. Indeed, as the molecules are given the same initial kinetic energy as the atoms (in our atomic impact models), the individual atoms obtained after dissociation have less momentum and hence a lower velocity than the ones generated in the atomic impacts and will therefore not penetrate as deep in the surface as the oxygen atoms issued from the atomic bombardment.

The analysis of the penetration probability distributions reveals that the implanted oxygen atoms preferentially reside in or close to the silicon layer planes rather than in between the silicon sheets, as illustrated in Figure 3 for the atomic oxygen impacts at 5 eV. Indeed, while at thermal energy the atom reacts with the surface and resides on the uppermost and in the first subsurface layer, the hyperthermal ones can penetrate deeper as they can surmount the corresponding energy barriers.[8] As can be seen in Figure 3, the atoms that are located at the topmost layer or in the first subsurface layer are only found on the top side of these layers. In contrast, oxygen atoms residing deeper in the crystal are found on both sides of the silicon layers. This behavior is strongly bound to the structure of the silicon surface. Indeed, the distributions show that the oxygen atoms have a low probability of being located under a reconstructed dimer on the terrace of the Si(100)$\{2 \times 1\}$ surface, as indicated by the absence of oxygen peaks at the left-hand side of the first two Si peaks at the surface, which is consistent with the fact that the chemisorbed atoms in the top layer and in the first subsurface layer cannot migrate between atoms of the silicon dimer.[13]

2. Impact-Induced Damage. Perhaps of even greater importance for material scientists than the actual penetration depth of the oxygen atoms is the damage that they induce in the Si-crystal due to their impact. In an effort to quantify this event, we computed the energy-dependent damage in terms of the average
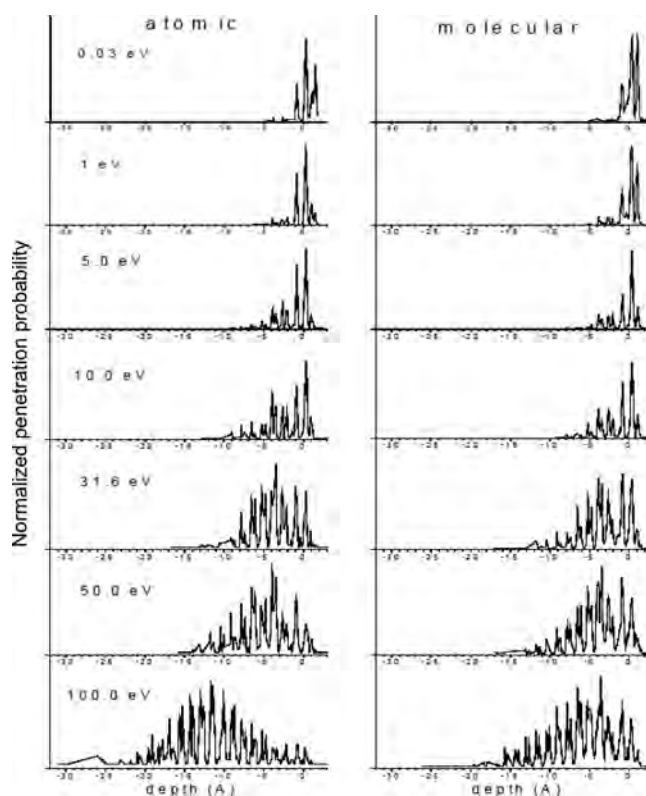
Figure 3. Calculated normalized penetration probability distribution of atomic oxygen with 5 eV impact energy in Si(100)$\{2 \times 1\}$ (black line). The gray peaks indicate the positions of the silicon layers. The top four Si layers are broader than the bulk layers due to the surface reconstruction. The depth = 0 Å position corresponds to the location of the surface dimer.

number of created *displaced* or *missing atoms* (MA) per impact (Figure 4).[35] For each atom i at position $\mathbf{r}_i$, the sum $\sum_j (\mathbf{r}_i - \mathbf{r}_j)$ of the vectors from i to all nearest neighbors j is calculated. If this sum is zero or very small, atom i is in a (near) perfect symmetrical environment and is considered to signal the absence of a point defect near i. However, if the magnitude of the sum is larger than a critical reference value, a MA is attributed to the position as

$$\mathbf{r}_{MA} = \mathbf{r}_i - \sum_j (\mathbf{r}_i - \mathbf{r}_j)$$

We use a value of 1.88 Å for the reference value, which is 80% of the nearest-neighbor distance in silicon. This allows us accounting for some structural or thermal disorders as compared to a perfect vacancy.

Both in the atomic and in the molecular case, the average number of MAs per impact steeply increases from 31.6 eV (Figure 4). Note that a few MAs are already created at 10 eV in the case of atomic impacts. At 31.6 eV, about 1 MA is created per impact, while this value increases to more than 2 at 100 eV.

Two distinct generation mechanisms of defects are observed in our calculations: the first one occurs through a simple knock-on displacement: when the impinging oxygen atom has sufficient kinetic energy, it can displace a Si-atom from its lattice location due to the collision, thereby creating a vacancy−interstitial pair (a Frenkel pair).[36] Note that the oxygen atom sets itself interstitially in this process. This event is only observed at high impact energy, i.e., above 10 eV, which is consistent with the experimentally observed energy window of 10−30 eV for the
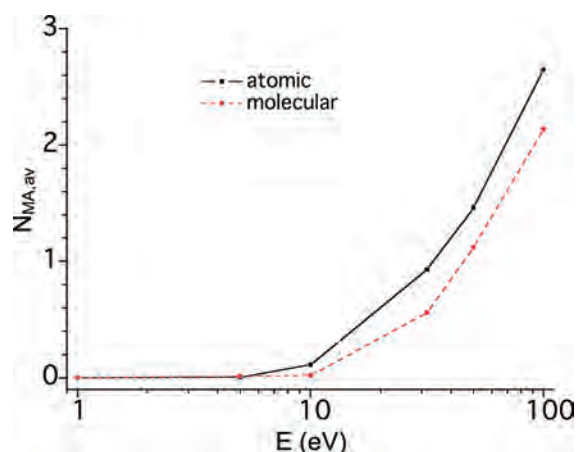
Figure 4. Calculated average number of missing atoms created in the Si-crystal per impact as a function of impact energy for atomic and molecular impacts.

Figure 5. Mechanism of defect creation by oxygen atom chemisorption at low impact energy below 10 eV.

displacement of Si,[34,37−39] as well as to the Frenkel pair energy threshold calculated by DFT for the [100] direction in Si (20 eV).[40]

In the second mechanism, the oxygen atom binds itself to two Si ones, forming a Si—O—Si bond. In some cases, a Si-atom (the upper one as seen from the surface) is pushed toward the surface and is displaced from its equilibrium lattice location (see Figure 5) and also creates a MA at that site.

In Figure 6, the distribution of the position of the impact-induced defects, or the location of the created vacancy, is depicted for different incoming energies, for both atomic and molecular impacts. Again, two energy regimes can be discerned: below and above 10 eV. Up to 10 eV, the impinging atom does not have enough energy to easily create a defect in the bulk of the structure. As a consequence, the created defects in this energy regime are all confined to the top layers of the crystal, especially in the first and second atomic layers. The incoming atom(s) will insert themselves into the Si—Si bond, thereby displacing the Si-atoms. This leads in a few cases to the creation of an atomic vacancy. Note, however, that the probability of this event to occur is small and ranges from 0.002 at 1 eV to 0.112 at 10 eV (see Figure 6). In this regime, the energy is too low to displace Si-atoms from their lattice positions, and knock-on displacements of Si-atoms do not take place. Hence, the interaction is limited to the chemisorption process.

At higher impact energies, the knock-on displacement of Si occurs through both primary and secondary knock-on mechanisms. The resulting defect distributions are shown in Figures 6 and 7. In Figure 6, besides the sharp peak around −2 Å, also a secondary broad distribution is observed around −5 to −10 Å for the atomic impacts. For the molecular impacts, depicted in Figure 7, the secondary distribution is visible until about −6 Å for the 31.6 eV case and until about −10 Å for the 100 eV case. Indeed, the initial impact, which usually displaces one or more Si-atoms in the top layers and which contributes to the peak at around −2 Å, slows down the impinging atom and subsequently sets it in an interstitial position into a Si—Si bond, creating a second defect in the underlying layer. Further, the impinging O-atom(s) also transfers a substantial amount of energy to the Si-atom in the collision. Indeed, the maximum energy that can be transferred in the O—Si collision is given by $T_{max} \equiv E_0(4m_1 m_2)/(m_1 \pm m_2)^2$, corresponding to about 92.5% of the initial impact energy
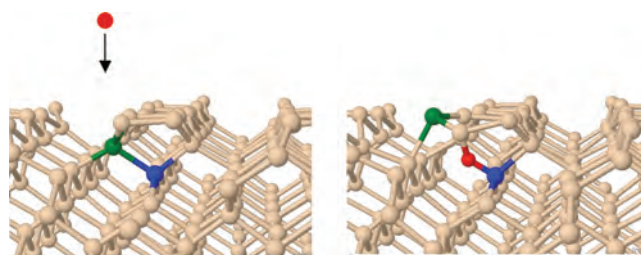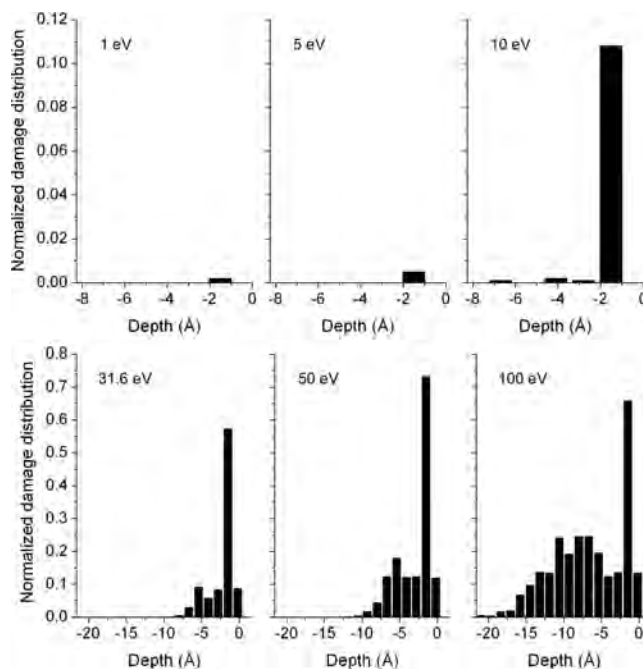
Figure 6. Distributions of the calculated damages, as a function of depth in the surface, for the different impact energies investigated (using atomic oxygen).

(or less). Therefore, secondary knock-on displacements can occur if the initial impact energy is sufficiently high, due to Si—Si collision cascades in the bulk of the structure. In this energy range, the total defect formation probability (composed of primary and secondary knock-on displacements) ranges from 0.92 (atomic case) and 0.56 (molecular case) at 31.6 eV impact energy to 2.65 (atomic case) and 2.14 (molecular case) at 100 eV impact energy.

Note that in the implantation process, the final location of the created defects and the final location of the implanted atom(s) are often found to be separated from each other by a considerable distance. This is illustrated in Figure 8 and in the accompanying movies (see Supporting Information), showing the impact of a 100 eV oxygen atom. The position of the oxygen atom (colored red) is shown every 6.25 fs; the positions of the silicon atoms are the final positions at the end of the trajectory. The darkness of the silicon atoms indicates the deviation of their final positions from their original positions, prior to the impact. In the process, the oxygen atom displaces a silicon atom of the fourth Si-layer from its lattice position (toward the left side in the figure, colored green in the movies). As explained above, the impinging O-atom
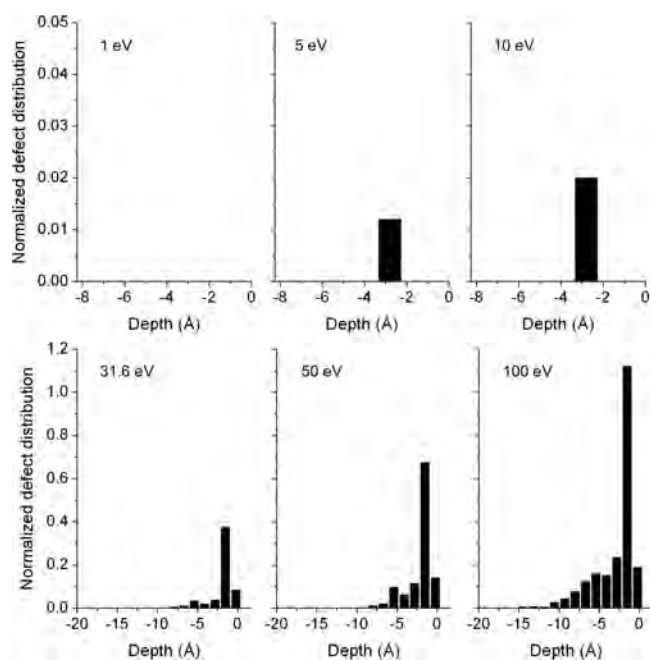
Figure 7. Distributions of the calculated damages, as a function of depth in the surface, for the different impact energies investigated (using molecular oxygen).
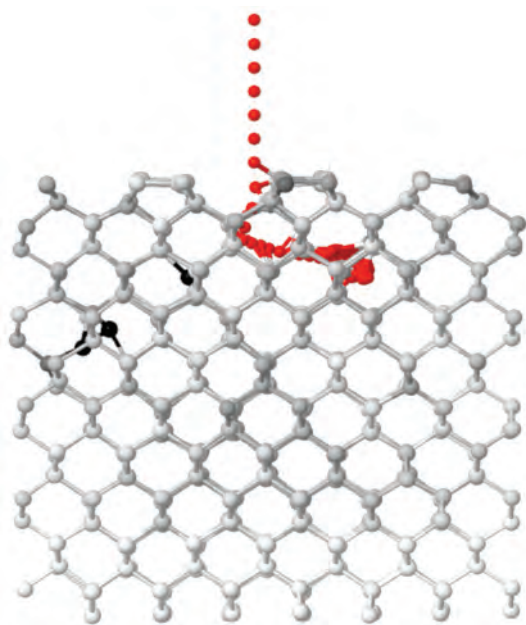
Figure 8. Illustration of the spatial separation between the location of the impact-induced defect (black Si-atoms, left side in the figure) and the implantation position of the O-atom (red atom, right side in the figure). The positions of the Si-atoms are plotted once, for the final configuration; the time interval between the consecutive positions of the impinging O-atom is 6.25 fs. The impact energy is 100 eV.

transfers a considerable amount of energy in the O—Si collision to this Si-atom, which can therefore displace another Si-atom. This Si-atom in turn becomes an interstitial in the lattice (colored blue in the movies). Meanwhile, the O-atom is deflected from the Si-atom nearly horizontally and travels through the lattice (to the

right side in the figure) until it has lost most of its kinetic energy. The distance between the implanted O-atom and the created defect in the final configuration is about 15 Å in this case.

■ SUMMARY AND CONCLUSIONS

Using reactive molecular dynamics simulations, we have investigated the probability of penetration of O_2 and single oxygen atoms generated through thermal and hyperthermal sources and the associated impact-induced damage in a $Si(100)\{2 \times 1\}$ surface. It is found that at low impact energies (i.e., lower or equal to 1.0 eV), the oxygen atoms remain confined to the surface layers and that the damage to the bulk is very limited and purely induced by the chemisorption process. At higher energies, the O-atoms can penetrate in the crystal to a depth of up to 20 Å. At these higher energies, the damages are much more pronounced, and primary and secondary knock-on displacements of Si are observed. This results in two distributions in the spatially resolved defect distributions.

■ ASSOCIATED CONTENT

ⓢ **Supporting Information.** (i) Movie showing the impact of a 100 eV O-atom impinging on the $Si(100)\{2 \times 1\}$ substrate, side view (without perspective depth); (ii) same impact, side view (with perspective depth); (iii) same impact, top view. These movies correspond to the defect formation process shown in Figure 8. The oxygen atom is colored red; all other atoms are Si. This material is available free of charge via the Internet at http://pubs.acs.org.

■ REFERENCES

(1) Wang, J.; Roman, P.; Kamieniecki, E.; Ruzyllo, J. *Electrochem. Solid-State Lett.* **2003**, *6*, G63–G65.

(2) Osipov, A. V.; Patzner, P.; Hess, P. *Appl. Phys. A: Mater. Sci. Process.* **2006**, *82*, 275–280.

(3) Teraoka, Y.; Yoshigoe, A. *Surf. Sci.* **2002**, *507*, 797–802.

(4) Yoshigoe, A.; Teraoka, Y. *Surf. Sci.* **2003**, *532*, 690–697.

(5) Enta, Y.; Mun, B. S.; Rossi, M.; Ross, P. N.; Hussain, Z., Jr.; Fadley, C. S.; Lee, K.; Kim, S. *Appl. Phys. Lett.* **2008**, *92*, 012110.

(6) Green, M. A. *Nanotechnology* **2000**, *11*, 401–405.

(7) Tagawa, M.; Yokota, K.; Tsumamoto, S.; Sogo, C.; Yoshigoe, A.; Lee, K. *Appl. Phys. Lett.* **2007**, *91*, 033504.

(8) Kisa, M.; Minton, T. K.; Yang, J. C. *J. Appl. Phys.* **2005**, *97*, 023520.

(9) Murad, E. *J. Spacecr. Rockets* **1996**, *33*, 131–136.

(10) Engstrom, J. R.; Engel, T. *Phys. Rev B* **1990**, *41*, 1038–1041.

(11) Engstrom, J. R.; Nelson, M. M.; Engel, T. *J. Vac. Sci. Technol., A* **1989**, *7*, 1837–1840.

(12) Engel, T. *Surf. Sci. Rep* **1993**, *18*, 91–144.

(13) Watanabe, H.; Kato, K.; Uda, T.; Fujita, K.; Ichikawa, M.; Kawamura, T.; Terakura, K. *Phys. Rev. Let.* **1998**, *80*, 345–348.

4822

dx.doi.org/10.1021/jp112068z |*J. Phys. Chem. C* 2011, 115, 4818–4823

(14) Ferguson, B. A.; Reeves, C. T.; Mullins, C. B. *J. Chem. Phys.* **1999**, *110*, 11574–11584.

(15) Miyake, T.; Soeki, S.; Kato, H.; Nakamura, T.; Namiki, A.; Kamba, H.; Suzaki, T. *Phys. Rev B* **1990**, *42*, 11801–11807.

(16) Hoshino, T.; Tsuda, M.; Oikawa, S.; Ohdomari, I. *Phys. Rev. B* **1994**, *50*, 14999–15008.

(17) Gusev, E. P.; Lu, H. C.; Gustafsson, T.; Garfunkel, E. *Appl. Surf. Sci.* **1996**, *104/105*, 329–334.

(18) Kato, K.; Uda, T. *Phys. Rev. B* **2000**, *62*, 15978–15988.

(19) Mazzone, A. M. *Eur. Phys. J. B* **2003**, *35*, 125–132.

(20) Massoud, H. Z. *Microelectron. Eng.* **1995**, *28*, 109–116.

(21) Quinteros, C. L.; Tzvetkov, T.; Jacobs, C. C. *J. Chem. Phys.* **2000**, *113*, 5119–5121.

(22) Gusev, E. P.; Lu, H. C.; Gustafsson, T.; Garfunkel, E. *Phys. Rev. B* **1995**, *52*, 1759–1775.

(23) Stefanov, B.; Raghavachari, K. *Surf. Sci.* **1997**, *389*, L1159–L1164.

(24) van Duin, A. C. T.; Dasgupta, S.; Lorant, F.; Goddart, W. A., III. *J. Phys. Chem. A* **2001**, *105*, 9396–9409.

(25) Abell, G. C. *Phys. Rev. B* **1985**, *31*, 6184–6196.

(26) Mortier, W. J.; Ghosh, S. K.; Shankar, S. *J. Am. Chem. Soc.* **1986**, *108*, 4315–4320.

(27) van Duin, A. C. T.; Baas, J. M. A.; van de Graaf, B. *J. Chem. Soc., Faraday Trans.* **1994**, *90*, 2881–2895.

(28) van Duin, A. C. T.; Strachan, A.; Stewman, S.; Zhang, Q.; Xu, X.; Goddard, W. A., III. *J. Phys. Chem. A* **2003**, *107*, 3803–3811.

(29) Buehler, M. J.; van Duin, A. C. T.; Goddard, W. A., III. *Phys. Rev. Let.* **2006**, *96*, 095505.

(30) Ning, N.; Calvo, F.; van Duin, A. C. T.; Wales, D. J.; Vach, H. *J. Phys. Chem. C* **2009**, *113*, 518–523.

(31) Fogarty, J. C.; Aktulga, H. M.; Grama, A. Y.; van Duin, A. C. T.; Pandit, S. *J. Chem. Phys.* **2010**, *132*, 174704.

(32) Valentini, P.; Schwartzentruber, T. E.; Cozmuta, I. *J. Chem. Phys.* **2010**, *133*, 084703.

(33) Mueller, J. E.; van Duin, A. C. T.; Goddard, W. A., III. *J. Phys. Chem. C* **2010**, *114*, 5675–5685.

(34) Dereli, G.; Yalabik, M. C.; Ellialtioglu, S. *Phys. Scr.* **1989**, *40*, 117–121.

(35) Timonova, M.; Groenewegen, J.; Thijsse, B. J. *Phys. Rev. B* **2010**, *81*, 144107.

(36) Loferski, J.; Rappaport, P. *Phys. Rev.* **1958**, *111*, 432–439.

(37) Corbett, J. W.; Watkins, G. D. *Phys. Rev.* **1965**, *138*, A555–A560.

(38) Hemment, P.; Stevens, P. *J. Appl. Phys.* **1969**, *40*, 4893–4901.

(39) Marton, D. In *Low Energy Ion−Surface Interactions*; Rabalais, J. W., Ed.; Wiley: Chester, U.K.; 1994; p 526.

(40) Holmström, E.; Kuronen, A.; Nordlund, K. *Phys. Rev. B* **2008**, *78*, 045202.